Ultrafast low-temperature metal–insulator interface phonon dynamics and heat transport in a Pt/$Gd_3Fe_5O_{12}$ heterostructure

Cite as: Struct. Dyn. **12**, 065101 (2025); doi: 10.1063/4.0000778
Submitted: 25 July 2025 · Accepted: 7 November 2025 ·
Published Online: 24 November 2025

Deepankar Sri Gyan,[1] Ni Li,[1] Zhantao Chen,[2,3] Stephan Geprägs,[4] Maxim Dietlein,[4,5] Rudolf Gross,[4,5,6] Takahiro Sato,[3] Yanwen Sun,[3] Matthias C. Hoffmann,[3] Diling Zhu,[3] Daniel Haskel,[7] Jörg Strempfer,[7] Mingda Li,[8] Danny Mannix,[9,10] and Paul G. Evans[1,a)]

AFFILIATIONS

[1]Department of Materials Science and Engineering, University of Wisconsin-Madison, Madison, Wisconsin 53706, USA
[2]Stanford Institute for Materials and Energy Sciences, Stanford University, Stanford, California 94305, USA
[3]Linac Coherent Light Source, SLAC National Accelerator Laboratory, Menlo Park, California 94025, USA
[4]Walther-Meißner-Institut, Bayerische Akademie der Wissenschaften, 85748 Garching, Germany
[5]School of Natural Sciences, Technical University of Munich, 85748 Garching, Germany
[6]Munich Center for Quantum Science and Technology (MCQST), Schellingstraße 7, 80799 München, Germany
[7]Advanced Photon Source, Argonne National Laboratory, Lemont, Illinois 60439, USA
[8]Department of Nuclear Science and Engineering, Massachusetts Institute of Technology, Cambridge, Massachusetts 02139, USA
[9]Université Grenoble Alpes, CNRS, Institut Néel, 38042 Grenoble, France
[10]European Spallation Source, SE-22100 Lund, Sweden

[a)]**Author to whom correspondence should be addressed:** pgevans@wisc.edu

ABSTRACT

Interfacial thermal and acoustic phenomena have an important role in quantum science and technology, including in spintronic and spincaloritronic materials and devices. Simultaneous measurements of the low-temperature thermal and acoustic properties of a metal/insulator heterostructure reveal distinct dynamics in the characteristic phonon frequency ranges of acoustic and thermal transport. The measurements probed a heterostructure consisting of a thin film of Pt on the ferrimagnetic insulator gadolinium iron garnet ($Gd_3Fe_5O_{12}$, GdIG) grown epitaxially on a gadolinium gallium garnet substrate. Ultrafast structural dynamics within the Pt layer were tracked using time-resolved ultrafast x-ray diffraction and analyzed to probe interfacial acoustic and thermal properties. The rapid heating of the Pt layer by a 400 nm wavelength femtosecond-duration optical pulse produced transient structural changes that provided the stimulus for these measurements. Rapid heating produced a broadband acoustic pulse that was partially reflected by the Pt/GdIG interface. Temporal frequencies up to 740 GHz, corresponding to angular frequencies of several THz, were detected in a wavelet analysis of the acoustic oscillations of the strain in the Pt layer. The structural results were analyzed to determine (i) the acoustic damping coefficient and phonon mean free path in Pt at frequencies of hundreds of GHz and (ii) the Grüneisen anharmonicity parameter. The thermal conductance of the Pt/GdIG interface was tracked using the slower, tens-of-picosecond-scale, dynamics of the initial cooling of the heated Pt layer. Analysis using a model based on the Boltzmann transport equation shows that the phonon transmission is lower at the phonon frequencies relevant to thermal transport than for subterahertz regime acoustics.

I. INTRODUCTION

Thin-film heterostructures present a range of possibilities to understand thermal and acoustic transport and ultimately to control these properties. Acoustic and thermal phenomena are deeply linked to each other and fundamentally include the transport and scattering of phonons within the layers and at interfaces.[1] Interfaces in heterostructures can also feature discontinuities in bonding and transport mechanisms that involve, for example, conversion between electronic

and vibrational mechanisms of thermal transport.[2] These phenomena are highly challenging many-body physics problems that have motivated the development of synthesis, experimental, and theoretical methods that extend the limits of the present understanding of transport and scattering processes.[3–8] Among these approaches are machine-learning techniques that help to refine fundamental parameters based on input from experiments.[9] The development of ultrafast time-resolved x-ray scattering methods is extending the range of phonon frequencies and mode-specific lifetimes that can be probed in nanostructured materials into the THz frequency regime/picosecond time regime.[10,11] At present, pulsed x-ray light sources including hard x-ray free-electron lasers, laser plasma sources, and spontaneous emission accelerator-based sources have sufficiently high intensity to allow these measurements to be performed in reasonable experimental times.[12–14]

Characterizing the low-temperature thermal transport and vibrational properties of nanoscale materials is particularly challenging. A time-domain approach can be highly valuable because the largest contribution of phonons to heat transport occurs for vibrational modes with frequencies on the order of 1 THz or less.[15] Processes in this THz regime overlap the bandwidth of the spectrum of the acoustic pulse produced by the absorption of a femtosecond-duration optical pulse.[16] Ultrafast time-resolved diffraction studies using x rays and electrons both have femtosecond-scale time resolution and provide the means to track heat transport through nanoscale layered structures with time resolution matching the fundamental acoustic and thermal transport timescales.[17,18] The experiments and analysis presented here focus on the Pt layer of a Pt/complex oxide heterostructure and capture its heating and cooling, and the acoustic oscillations resulting from a photothermally generated strain pulse. The thermal and acoustic analysis yields the acoustic damping coefficient and phonon mean free path, the acoustic mismatch between the Pt and oxide layers, the Grüneisen anharmonicity parameter in Pt, and the Pt/oxide interfacial thermal conductance. The experimental results also provide insight into microscopic phonon transport parameters based on further analysis using a complementary Boltzmann transport equation approach.[9]

We report the low-temperature thermal and acoustic properties of a thin-film heterostructure consisting of a 75 nm-thick epitaxial thin film of gadolinium iron garnet ($Gd_3Fe_5O_{12}$, GdIG) and a polycrystalline 13.2 nm Pt capping layer on a (111)-oriented gadolinium gallium garnet ($Gd_3Ga_5O_{12}$, GGG) substrate.[19] The Pt/GdIG/GGG system is of interest in the study of the spin-Seebeck effect (SSE) and related phenomena, in which magnetic and thermal phenomena are coupled.[19] Thermal transport at low temperatures underpins spincaloritronic and thermoelectric phenomena.[19,20] The temperature regime considered here, 20–130 K, is particularly relevant to SSE phenomena because the SSE exhibits a sign reversal in this temperature range.[19] Experiments in the low-temperature regime can be challenging because there are significant nonmonotonic temperature dependences of structural and magnetic parameters.[19]

The experiments presented here use ultrafast x-ray diffraction, as shown in Fig. 1(a). The Pt layer is heated by optical pump pulses synchronized with a variable delay with respect to hard x-ray pulses from the Linac Coherent Light Source (LCLS) free-electron laser. The femtosecond-duration ultrafast optical pulse, Fig. 1(a), had a duration of approximately 50 fs. Further experimental details are given in Sec. II.

The laser heating rapidly raises the temperature of the Pt layer by up to hundreds of degrees for the optical fluences used in these experiments. The optical absorption coefficient at 400 nm for GdIG was far less than for Pt.[21,22] At early times after optical excitation, on the order of less than 10 ps, the GdIG layer beneath the Pt thus remains close to its initial temperature because (1) there is low optical absorption in the GdIG and (2) a large temperature difference arises from the finite thermal conductance of the Pt/GdIG interface.

The rapid heating of the Pt layer produces multiple effects that are apparent in the x-ray diffraction experiments. First, thermal expansion of the Pt layer leads to an increase in its lattice parameter. Second, the temperature increase in the Pt layer and its subsequent thermal expansion launch an acoustic strain pulse in the Pt layer that is transmitted into the GdIG thin film. This acoustic pulse is generated due to the momentum associated with the expansion of the Pt. Structural features of the Pt layer, including the lattice parameter and the Debye–Waller effect, then have picosecond-scale dynamics from which vibrational and thermal parameters can be extracted. The structural perturbations have a timescale set by the thickness of the layers and the acoustic velocity, on the order of 5 ps, and extending to tens of picoseconds. Thermal transport after excitation occurs at a longer timescale, with the maximum temperature of the GdIG layer expected at approximately 200 ps.[18]

The experiments presented here probe thermal and acoustic properties in a different regime than previous studies. Time-resolved x-ray diffraction studies of thin Pt foils have been used to probe the room-temperature electron–phonon coupling coefficients and to provide a measurement of the time over which the expansion of the lattice occurs.[23] Experiments reported by Zahn *et al.* used a freestanding Pt layer and thus did not probe acoustic transmission and thermal conductance at a Pt/substrate interface.[23] An earlier study of thermal transport in this system probed thermal transport using changes in the x-ray reflection from the GdIG component of the Pt/GdIG system.[18] The use of a GdIG x-ray reflection to study the dynamics was required at that time because of the limited x-ray dynamic range available in the previous x-ray measurements, which were also made without sufficient time resolution to resolve acoustic effects.[18] Calculations of interfacial thermal transport properties based on the acoustic mismatch model (AMM) and diffusive mismatch model (DMM) are widely used to predict the phonon transport through the interfaces.[24] These models do not account for the interaction among the local vibration modes at the interfaces between two different materials and hence cannot predict the interfacial phonon transport properties of the interfaces.[24] The experimental measurement of parameters influencing the phonon transport properties of the interfaces is crucial for caloritronic devices.

II. METHODOLOGY

The optical pump x-ray probe diffraction experiment was performed at the x-ray pump probe beamline of the LCLS, using the arrangement shown in Fig. 1(a).[12] A collinear geometry was employed for the optical pump and x-ray probe pulses. The spot sizes for the optical pump and x-ray probe were 130×400 μm^2 and 30×60 μm^2, respectively. The x-ray probe pulses had a photon energy of 7.935 keV and a repetition rate of 120 Hz. Optical pulses had a wavelength of 400 nm (photon energy 3.1 eV). X-ray diffraction patterns were recorded with specific delay times Δt after the optical pulses. The arrival time of each x-ray pulse relative to the optical pulses was characterized using the LCLS time tool instrument with an approximate time resolution of 10 fs.[25] The effective time resolution of the measurement depended on a combination of the steps selected in the experimental scans and on the binning of the arrival

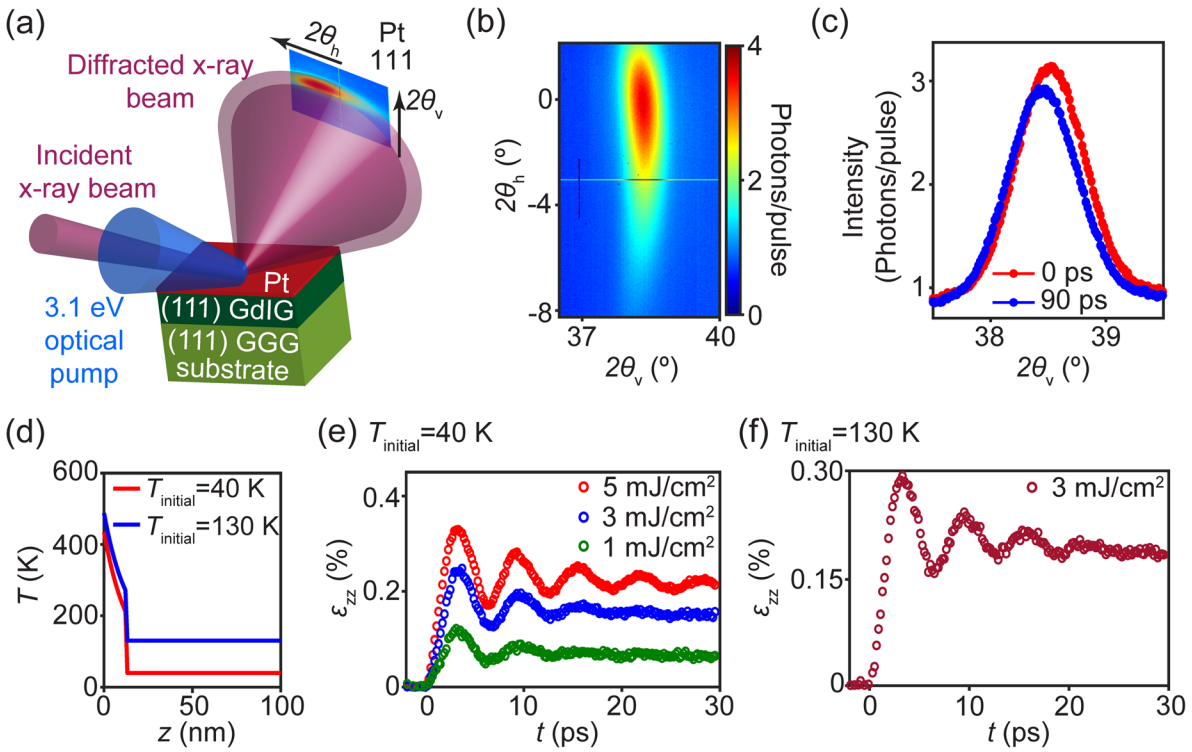

FIG. 1. (a) Optical pump/x-ray probe study of transient structural effects in the Pt component of a Pt/GdIG/GGG heterostructure. (b) Diffracted intensity distribution of the Pt 111 reflection averaged over 100 x-ray pulses with a photon energy of 7.935 keV without optical excitation. The horizontal and vertical lines near −3.5° and 37°, respectively, are artifacts resulting from the boundary between adjacent panels of the x-ray detector. (c) Shift in $2\theta_v$ and change in intensity of the Pt 111 reflection between diffraction patterns acquired before optical excitation and at 90 ps after optical excitation. (d) Temperature of the Pt layer, computed using the model described in the text, at a time immediately after optical excitation for $T_{initial} = 40$ and 130 K. Measured time dependence of the longitudinal strain, ε_{zz}, computed from the interplanar spacings of the Pt 111 reflection for (e) $T_{initial} = 40$ K, and (f) $T_{initial} = 130$ K.

time selected during the analysis. The data presented span the range of values of Δt from 0 to 30 ps, for which the analysis focused on acoustic propagation, and 0–90 ps, with the analysis focusing on longer-timescale thermal transport.

The optical absorption lengths for Pt and GdIG at 400 nm are 10 and 360 nm, respectively.[21,22] The repetition rate of the optical pump matched the 120 Hz repetition rate of the x-ray probe pulses. The experiments were conducted with a fixed x-ray incident angle of 25.07° with respect to the sample surface. The experiment was carried out at initial temperatures $T_{initial}$ of 40 and 130 K. At 40 K, the measurement was performed with optical fluences of 1, 3, and 5 mJ cm^{-2}. At 130 K, the measurement was performed with 3 mJ cm^{-2} optical fluence. A summary of the literature values of parameters used in the analysis here and below is given in Table I.

III. RESULTS AND DISCUSSION

A. Acoustic strain generation and propagation

A Pt diffraction pattern acquired by averaging the signal from 100 x-ray pulses without optical excitation at an initial sample temperature $T_{initial} = 40$ K is shown in Fig. 1(b). The Pt 111 diffraction ring has a maximum intensity along the surface-normal direction that arises from the crystallographic texture of the Pt layer. The diffracted intensity is plotted in Fig. 1(b) as a function of two diffraction angles, $2\theta_v$ and $2\theta_h$. The $2\theta_v$ angle spans the conventional 2θ angle of thin-film diffraction. The angle $2\theta_h$ spans an azimuthal direction along the Pt powder diffraction ring. The Pt 111 diffraction ring exhibited a broad azimuthal maximum along $2\theta_h$ with a full width at half maximum (FWHM) of 6.2°. The zero of $2\theta_h$ was set using the GdIG x-ray reflection of the GdIG layer, and the intensity distribution along $2\theta_h$ in Fig. 1(b) is thus slightly offset from $2\theta_h = 0$. The apparent (111) texture of the Pt layer is consistent with expectations for face-centered cubic metals deposited on oxide substrates.[35] The distribution of intensity in the 111 ring had an angular FWHM in the $2\theta_v$ scattering angle of 1.4°. The size of the crystallites contributing to this width given by a Scherer analysis was 16.5 nm, approximately matching the thickness of the Pt layer. The Pt thin film thus consisted of (111)-oriented crystallites extending through the entire depth of the film.

The analysis of thermal and acoustic effects in the Pt layer was based on measurements of d_{111}, the interplanar spacing of the (111) planes. This spacing is discussed below in terms of the longitudinal component of the elastic strain ε_{zz}, defined as $\Delta d_{111}/d_{111}$. The longitudinal strain was measured using the angular shift of the Pt 111 reflection, using a fit of a Gaussian function to the distribution of the diffracted intensity from Pt (111) planes along $2\theta_v$, extracting Δd_{111} from the shifts in $2\theta_v$. Heating results in a shift in $2\theta_v$ due to thermal expansion and a decrease in intensity due to the Debye–Waller effect.

TABLE I. Summary of literature values of parameters used in the calculations.

Quantity	Symbol	Value	Reference
Specific heat capacity	C_P	Temperature dependent	26, 27
Optical absorption length in Pt	ξ	10 nm	22
Pt Poisson ratio	ν_{Pt}	0.39	28
Pt longitudinal acoustic sound velocity (literature)	v_{Pt}	3920 m s^{-1}	28
GdIG longitudinal acoustic sound velocity	V_{GdIG}	6500 m s^{-1}	29
Elastic shear modulus of Pt	G_{Pt}	53 GPa	30
Debye temperature of Pt	$T_{D,Pt}$	246 K	31
Mass density of Pt	ρ_{Pt}	21.45 g cm^{-3}	28
Volume per Pt atom	$V_{0,Pt}$	1.51×10^{-23} cm^{-3}	Based on[28]
Mass density of GdIG	ρ_{GdIG}	7.08 g cm^{-3}	29
Electron effective mass in Pt	m_{Pt}^*	1.18×10^{-29}	32
Optical reflectivity of Pt at 400 nm	R	0.4	33
Grüneisen parameter for Pt	γ_{Pt}	2.5	34

Both are apparent in the comparison of the intensity distributions as a function of $2\theta_v$ just before optical excitation and 90 ps after optical excitation in Fig. 1(c). The intermediate times, described later in this section, also include effects arising from the propagation of an acoustic strain pulse.

Figure 1(d) shows the initial state of the time-dependent simulation of the thermal profile as a function of depth for a time immediately after optical excitation. The depth profile of the temperature, shown in Fig. 1(d), was calculated from the energy absorbed per unit volume in the Pt layer, given by $W(z) = \frac{(1-R_{Pt})F}{A\xi} e^{-z/\xi}$, where R_{Pt} is the optical reflectivity of Pt, F is the optical fluence, A is the illuminated area, and ξ is the optical absorption length in Pt. The heat required to raise the temperature from $T_{initial}$ to $T(z,t=0)$ is given by $W(z) = \int_{T_{initial}}^{T(z,t=0)} \rho C_P(z,T)dT$, where $C_P(z, T)$ is the depth- and temperature-dependent specific heat capacity. This equation was numerically solved to find $T(z,t=0)$. The value of ρ was taken to be constant, which makes the use of C_P without correction for expansion appropriate. The optical absorption properties of Pt and the temperature-dependent specific heat were obtained from previous reports.[22,26,27] The simulation in Fig. 1(d) was performed for an optical fluence of 3 mJ cm^{-2} with $T_{initial} = 40$ and 130 K, matching one set of optical excitation parameters. The increase in temperature for the same optical fluence at $T_{initial} = 130$ K is less than that for $T_{initial} = 40$ K due to the increase in the heat capacity of Pt as a function of temperature.

A measurement of ε_{zz} as a function of time after optical excitation at an initial temperature of $T_{initial} = 40$ K is shown in Fig. 1(e) for three values of the optical fluence. At $t = 0$, immediately after optical excitation, the heated Pt layer retains the initial lattice parameter and has a large thermal stress that induces the subsequent expansion.[16] The expansion begins at the free surface of the film and propagates to the film/substrate interface. More specifically, ε_{zz} shows a rapid rise after $t = 0$ and reaches a maximum at $t = 3.4$ ps. In addition to the overall thermal expansion, ε_{zz} exhibits acoustic oscillations with a frequency determined by the thickness of the Pt layer, L_z, and the longitudinal acoustic sound velocity v_{Pt}. After $t = 3.4$ ps, ε_{zz} oscillates and the amplitude of oscillations decays with time. The time dependence of ε_{zz} shows this oscillatory behavior for all values of the optical fluence. The time dependence of the strain for $T_{initial} = 130$ K, Fig. 1(f), is qualitatively similar to $T_{initial} = 40$ K.

The experimentally observed acoustic strain was compared with a model of acoustic propagation. Temperature-dependent literature values of the specific heat and the thermal expansion coefficient, adjusted to account for a mechanical boundary condition at the GdIG/Pt interface, were used to provide an initial estimate of the magnitude of the strain pulse based on the thermal caculation.[26,27,34,36,37] The simulations employed the bulk Poisson ratio of Pt, $\nu_{Pt} = 0.39$.[26,28] Possible effects arising from substrate clamping of the in-plane lattice parameters were not included in the simulations. The acoustic model considered a strain pulse originating from the surface of the Pt film traveling toward the Pt/GdIG interface, and reflections from the Pt/GdIG and Pt/vacuum interfaces. After reaching the interface, a fraction of the energy in the acoustic strain pulse propagated through the interface, and the remainder was reflected into the Pt film. In a continuum acoustic model, the transmission and reflection depend on the acoustic impedance mismatch and set by the densities and sound velocities of the layers.[38] The acoustic impedance mismatch at the Pt/GdIG interface is[38]

$$Z_{Pt/GdIG} = \frac{\rho_{GdIG} v_{GdIG}}{\rho_{Pt} v_{Pt}}.$$

Here, ρ_i and v_i are the density and the longitudinal acoustic sound velocity of layer i, respectively. The reported room-temperature values of v_{Pt} and ρ_{Pt} are 3920 m s^{-1} and 21.45 g cm^{-3}, respectively.[26,28] For GdIG, the reported values for the acoustic velocity and density are $v_{GdIG} = 6500$ m s^{-1} and $\rho_{GdIG} = 7.08$ g cm^{-3}, respectively.[29] We have used these room-temperature values as the starting point for the acoustic simulations. The acoustic impedance mismatch for the Pt/GdIG interface calculated from these values is 0.55.

B. Acoustic damping and phonon mean free path

We define the acoustic phonon damping coefficient for the Pt layer to be ζ_{Pt}, the inverse of the time constant of the exponential decay of the acoustic amplitude. The continuum acoustic simulation includes (1) the generation, propagation, and reflection of the strain pulse arising from optical absorption in the Pt layer; (2) the damping factor, $e^{-\zeta_{Pt}t}$; and (3) the comparatively long-timescale thermal transport from heated Pt into the GdIG layer. The phase of the strain pulse reflected into the Pt layer from the Pt/GdIG interface depends on the densities of the two layers. The density of Pt is higher than the density of GdIG, and the reflection thus occurs with a 180° phase change. The reflected pulse travels through the Pt layer to the surface and is reflected by the Pt vacuum interface, again with a 180° phase change. The reflection repeats until the amplitude of the oscillating acoustic strain decays due to the combined effects of acoustic damping within the Pt layer and of acoustic transmission through the Pt/GdIG

interface. The effect of damping was empirically included in the model by multiplying the strain amplitude at every spatial point by $e^{-\zeta_{Pt}t}$, similar to an approach previously applied in time-resolved reflectance studies of phonon and charge-carrier relaxation dynamics.[39,40]

The strain in the Pt layer exhibited a long-timescale decay during the conduction of the heat resulting from optical excitation into the substrate. The thermal relaxation is evident from the slow decay of the strain in Figs. 1(e) and 1(f). The long-timescale decrease in the strain in Figs. 1(e) and 1(f) corresponds to only on the order of 10% of the initial excitation after 30 ps because the thermal transport through the Pt/GdIG interface is impeded by the finite interfacial thermal conductance. The thermal transport behavior is discussed below.

Figure 2(a) shows a simulated map of ε_{zz} as a function of depth and time for an optical fluence of 3 mJ cm^{-2} at $T_{initial} = 40$ K. A comparison of the depth-averaged simulated strain as a function of time with the measured strain is shown in Fig. 2(b), showing good agreement. The simulated strain profile was compared with the experimental results by computing the depth-averaged strain in the Pt layer. An analysis of the simulation results in Figs. 2(a) and 2(b) shows that the time at which the first peak appears in the strain measurements in Figs. 1(e) and 1(f) corresponds to the time at which the strain pulse reached the Pt/GdIG interface. The reduction in the magnitude of the strain between 3.4 and 6.8 ps corresponds to an acoustic reflection with a 180° phase change at the interface. The strain decreases until the reflected pulse is reflected again from the surface. The longitudinal acoustic sound velocity in Pt was measured from the sequence of maxima in Figs. 1(e) and 1(f) and Fig. 2(b) is 3910 (±20) m s^{-1} for the temperature $T_{initial} = 40$ K, very close to the reported bulk Pt acoustic velocity 3920 m s^{-1}.

Harmonic analysis of the time dependence of the strain was conducted using continuous wavelet transform (CWT). The CWT was performed using a predefined function in MATLAB R2022a (MathWorks, Inc.) using a Morse wavelet.[41,42] The CWT amplitude plotted in an angular frequency–time (ω-t) space in Fig. 2(c) shows higher harmonics of the frequency corresponding to the acoustic transit time. The wavelet transform analysis reveals mechanical oscillations at frequencies up to at least 740 GHz, the fourth harmonic of the frequency of the fundamental acoustic oscillation frequency.

A further complication arises because the acoustic pulse propagates in the heated Pt layer. The average effective temperature T_{eff} of the Pt layer for each value of $T_{initial}$ for several optical fluences is plotted in Fig. 3(a). The temperature of the Pt layer following optical excitation of 3 mJ cm^{-2}, for example, was $T_{eff} = 340$ K for $T_{initial} = 40$ K and $T_{eff} = 407$ K for $T_{initial} = 130$ K. The acoustic pulse in Pt should thus be thought of as propagating at these high temperatures, instead of at $T_{initial}$.

The value of $Z_{Pt/GdIG}$ was determined by comparing the experimental results with simulations. The decrease in the strain from 3.4 to 6.8 ps provides a way to measure the amplitude fraction of the strain pulse reflected from the Pt/GdIG interface, given by $Z_{Pt/GdIG}$. The ratio of strain at $t = 3.4$ ps and $t = 6.8$ ps was used to determine $Z_{Pt/GdIG}$. Simulated values of the ratio of ε_{zz} at $t = 3.4$ ps to its value at $t = 6.8$ ps were computed from simulations for several values of $Z_{Pt/GdIG}$. The minimum root-mean-squared deviation (RMSD) between simulation and experiment was observed for $Z_{Pt/GdIG} = 0.37$ with $T_{eff} = 340$ K and $Z_{Pt/GdIG} = 0.39$ for $T_{eff} = 407$ K. The values of $Z_{Pt/GdIG}$ as a function of T_{eff} are plotted in Fig. 3(b). The uncertainty in the values of $Z_{Pt/GdIG}$

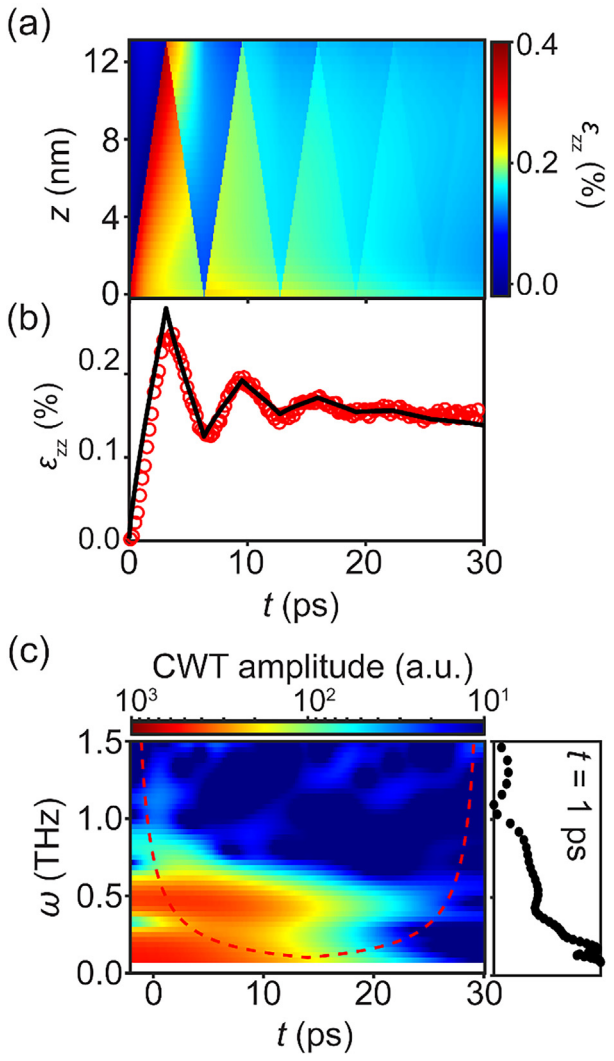

FIG. 2. (a) Simulated depth and time dependence of the strain ε_{zz} in the Pt layer. (b) Comparison of the time dependence of the measured strain ε_{zz} with simulated average strain based on the acoustic and thermal models for an optical fluence of 3 mJ cm^{-2} at $T_{initial} = 40$ K. (c) ω-t space map of the amplitude of the continuous wavelet transform (CWT) of the time dependence of the strain shown in (b). The right panel shows the line cut at $t = 1$ ps.

shown in Fig. 3(b) was estimated from the difference between the experimental data and the simulation. The values of $Z_{Pt/GdIG}$ range from approximately 0.28 to 0.45, lower than the predicted value of 0.55, possibly due to imperfections at the Pt/GdIG interface.

Under all experimental conditions, the strain reached an initial maximum at the same time, 3.4 ps. The experimental results do not exhibit a significant change of more than approximately 5% in the sound velocity as a function of temperature between $T_{eff} = 203$ K and $T_{eff} = 490$ K.

We have evaluated the simultaneous effect of acoustic damping within the Pt by comparing the relative magnitudes of successive extrema in the strain pulse, which exhibit an additional decrease

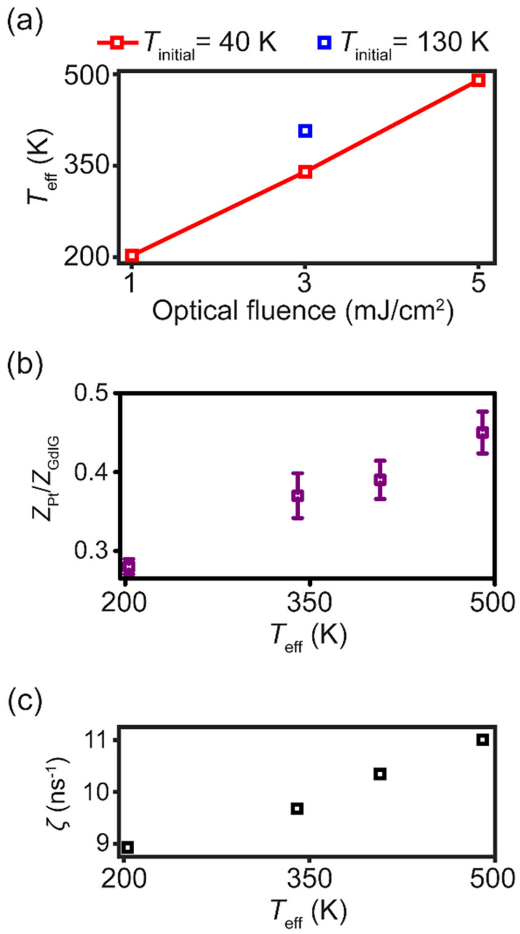

FIG. 3. (a) Simulated effective temperature T_{eff} of the Pt layer immediately after optical excitation as a function of optical fluence for experimental values of the $T_{initial}$. (b) Z_{Pt}/Z_{GdIG} as a function of T_{eff}. (c) Damping coefficient as a function of T_{eff}.

beyond the effects of acoustic transmission into the substrate. The acoustic phonon damping coefficient ζ_{Pt} was measured by comparing the average values of the neighboring maxima and minima in ε_{zz}. The decrease between successive maxima arises from the combined effects of the damping of the strain amplitude and acoustic transmission through the Pt/GdIG interface. The acoustic simulation was repeated for a range of values of ζ_{Pt}, and the corresponding average values of the neighboring maxima and minima were calculated for each simulation. The minimum RMSD was observed for $\zeta_{Pt} = 9.7$ and 10.3 ns^{-1} for $T_{eff} = 340$ and 407 K, respectively. The values of ζ_{Pt} as a function of T_{eff} are shown in Fig. 3(c).

Damping is often discussed in terms of a mean free path, defined to be the product of the relaxation time corresponding to the mean time between scattering events, and the acoustic sound velocity.[43] For the model here, the relaxation time is $1/\zeta_{Pt}$.[44] The value of the damping coefficient can be used to determine the phonon mean free path Γ_{Pt}, with $\Gamma_{Pt} = v_{Pt}/\zeta_{Pt}$.[45] The phonon mean free paths ranged from 444 nm at $T_{eff} = 200$ K to 355 nm at 490 K nm. The temperature dependence of the mean free path determined from the analysis is shown in Fig. 4.

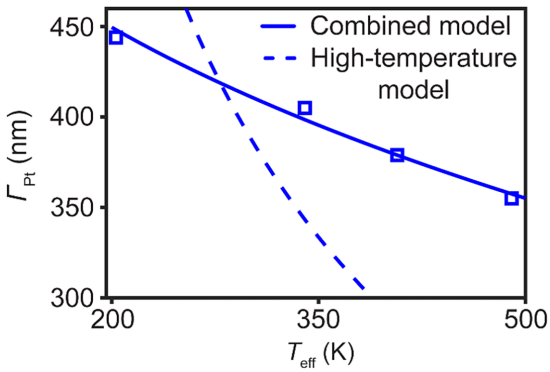

FIG. 4. Experimental mean free path measurements for several temperatures (points). Fits of the high-temperature approximation (dashed line) and a combination of high-temperature approximation and electron–phonon scattering (solid line).

The mean free path is greater than both the Pt thickness and the wavelength at the primary frequency of the longitudinal acoustic sound wave in the strain pulse.

Damping times in the few-ps to ten-ps range have been reported in optically pumped Ag and Au nanoparticles.[40,46] The damping time reported here, $1/\zeta_{Pt} = 90$–100 ps, is thus inconsistent with previous reports and perhaps arises because the Pt thin film forms a two-dimensional layer with comparatively smooth planar interfaces. In principle, longer damping times could be observed at lower temperatures. Low-temperature mean free paths in freestanding AuPd alloy layers are on the order of 25 nm.[47]

The Debye temperature of Pt is $T_{D,Pt} = 246$ K.[31] For temperatures much higher than $T_{D,Pt}$, the probability of Umklapp scattering is proportional to the effective phonon population.[43] Under these conditions, the dominant scattering rate relevant to the mean free path is inversely proportional to T.[48,49] The mean free path for Umklapp scattering in the equipartition limit at high temperatures, i.e., $T > T_{D,Pt}$, is[48,49]

$$\Gamma_{Pt}^{\text{Umklapp}} = \frac{G_{Pt} V_{o,Pt} f_{D,Pt} v_{Pt}}{4\pi\gamma^2 f^2 k_B} \frac{1}{T}. \quad (1)$$

Here, G_{Pt} is the elastic shear modulus, $V_{0,Pt}$ is the volume per Pt atom, $f_{D,Pt}$ is the Debye frequency, v_{Pt} is the phonon group velocity, k_B is the Boltzmann constant, f is the acoustic oscillation frequency, and γ_{Pt} is the Grüneisen anharmonicity parameter. A key point is that the acoustic propagation occurs in the optically heated layer at temperature $T = T_{eff}$. The effective temperature of the Pt layer for the fluences used with $T_{initial} = 40$ K is plotted in Fig. 3(a). The temperature of the Pt layer is approximately constant within 40 K over the time, in which the acoustic data were analyzed. An unconstrained best fit of the prediction based on this high-temperature model, plotted as a function of T_{eff} in Fig. 4 fails to explain the experimentally observed temperature dependence of the mean free path.

The phonon mean free path is also affected by the scattering of acoustic phonons by electrons. The electron–phonon scattering mean free path is $\Gamma_{Pt}^{e-ph} \propto e^{\frac{m^* v_{Pt}^2}{2k_B T}}$, where m^* is the electronic effective mass.[48] Since the high-temperature Umklapp approximation is not a good fit to the data, we have assumed that a combination of these two effects

contributes to the value of the mean free path. If multiple processes are involved, the net mean free path is given by Matthiesen's rule, $\frac{1}{\Gamma_{Pt}} = \frac{1}{\Gamma^a_{Pt}} + \frac{1}{\Gamma^b_{Pt}}$, where Γ^i_{Pt} is the contribution from process with index i.[43] The combined model for the mean free path is

$$\frac{1}{\Gamma_{Pt}} = k_1\, T + k_2\, e^{-\frac{m^*_{Pt} v^2_{Pt}}{2 k_B T}}. \quad (2)$$

Here $k_1 = \frac{4\pi {\gamma_{Pt}}^2 f^2 k_B}{G_{Pt} V_{o,Pt} f_{D,Pt} v_{Pt}}$, from Eq. (1), and k_2 is an unknown adjustable parameter describing the contribution of electron–phonon scattering. The temperature dependence of the mean free path was fitted using the combined model described above, shown in Fig. 4 for the values $k_1 = 1.84 \times 10^{-6}\,\mathrm{nm^{-1}\ K^{-1}}$, $k_2 = 0.002\,\mathrm{nm^{-1}}$, and ${m_{Pt}}^* = 1.28 \times 10^{-29}\,\mathrm{kg}$. The effective electron mass in Pt is reported as $1.18 \times 10^{-29}\,\mathrm{kg}$, which is close to the value of $1.28 \times 10^{-29}\,\mathrm{kg}$ derived from the temperature dependence.[32]

The measured value of k_1 was used to estimate the value of the Grüneisen anharmonicity parameter (γ_{Pt}) at the fundamental frequency of the acoustic pulse. The parameters for Pt used to calculate γ_{Pt} are $G_{Pt} = 53\,\mathrm{GPa}$,[30] $V_{o,Pt} = 60.467\,\mathrm{Å}^3$,[36] and $v_{Pt} = 3910\,\mathrm{m\,s^{-1}}$. The Debye frequency $f_{D,Pt}$ was calculated using $f_{D,Pt} = \frac{1}{2\pi}\left(\frac{6\pi^2 v^3_{Pt}}{V_{o,Pt}}\right)^{\frac{1}{3}}$, giving $f_{D,Pt} = 6.3\,\mathrm{THz}$.[43] In the low-frequency limit, the experimental values of γ for metals such as Au, Ag, and Cu determined from low-temperature thermal expansion data are ~3, ~2.2, and ~1.8, respectively.[50] The value of γ_{Pt} calculated from the low-temperature thermal expansion data is 2.5.[34] In our case, the product of the frequency and Grüneisen parameter is $\gamma_{Pt} f = 4.4 \times 10^{11}\,\mathrm{Hz}$. Taking $f = 170\,\mathrm{GHz}$, the principal frequency of the longitudinal acoustic strain pulse gives $\gamma_{Pt} = 2.6$, similar to the previous measurements for Pt and other metals.

C. Thermal transport and interfacial thermal properties

The thermal transport parameters of the Pt/GdIG were probed using the time dependence of the integrated intensity of the Pt 111 x-ray reflection. Figure 5(a) shows the time dependence of the intensity of the Pt 111 reflection measured for $T_{initial} = 40\,\mathrm{K}$ and 1 mJ cm^{-2} fluence, corresponding to $T_{eff} = 203\,\mathrm{K}$. Figure 5(a) spans 0 to 90 ps, a longer time range than the measurements in Figs. 1 and 2. The heat conducted into the substrate from the Pt layer during this time is on the order of tens of percent of the absorbed optical energy. The intensity shown in Fig. 5(a) decreases rapidly after $t = 0$ and then shows a slow relaxation toward the initial value. The uncertainty resulting from photon counting statistics in the intensity, shown as the error bars in Fig. 5(a), is smaller than the systematic changes in intensity due to heating.

Thermal diffusion simulations were conducted to understand the thermal transport behavior in the heterostructure. The thermal diffusion equations were solved using the forward Euler method.[51] The method was similar to our previous study of the dynamics of the lattice parameter of the GdIG layer.[18] Values of the thermal conductivities of Pt and GdIG for the simulations were taken from Refs. 52 and 53.

The key parameter for thermal transport from Pt to GdIG is the Pt/GdIG interfacial thermal conductance, $h_{Pt/GdIG}$. The temperature dependence of the interface thermal conductance is commonly described using a power-law model:[54]

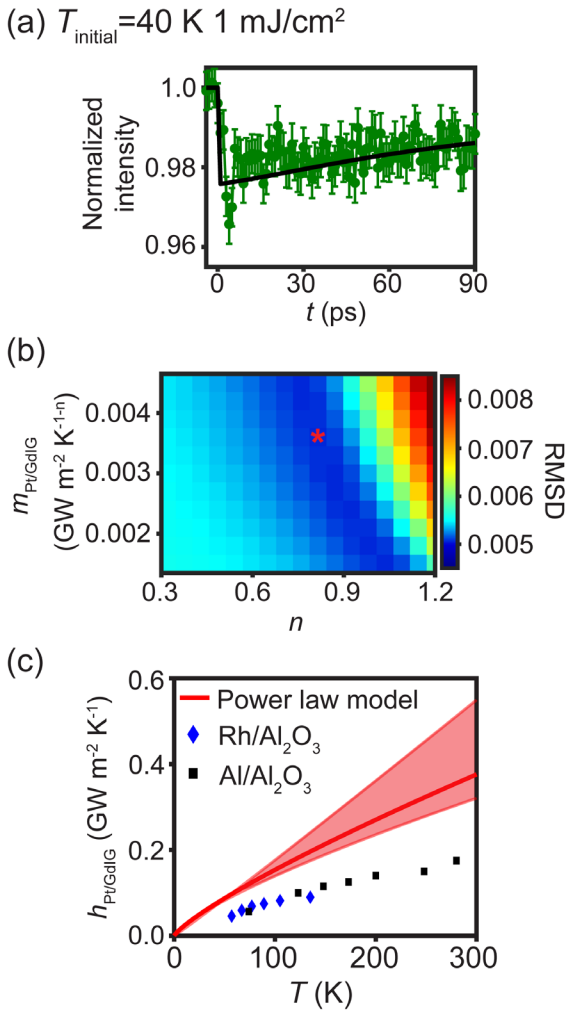

FIG. 5. (a) Measured (points) and calculated (lines) intensity of the Pt 111 x-ray reflection as a function of time, measured at $T_{initial} = 40\,\mathrm{K}$ with 1 mJ cm^{-2} optical fluence. (b) Root-mean-squared deviation (RMSD) of measured intensity and the intensity calculated using the Debye–Waller factor for the simulated thermal profile as a function of the parameters $m_{Pt/GdIG}$ and n of the model for the temperature dependence of the Pt/GdIG interface thermal conductance. (c) Pt/GdIG interface thermal conductance as a function of temperature according to the model using the parameters extracted from fitting the observed Pt 111 x-ray diffraction intensity. Literature values of the thermal conductance of Rh/Al$_2$O$_3$ and Al/Al$_2$O$_3$ interfaces are plotted for comparison.[57]

$$h_{Pt/GdIG} = m_{Pt/GdIG} T^n.$$

Here, n is a small scalar parameter and $m_{Pt/GdIG}$ is a constant.[54] The thermal diffusion equation was solved for a series of values of $m_{Pt/GdIG}$ and n to obtain the spatiotemporal temperature profile in the Pt layer. The comparison of the simulation with the measured integrated intensity was used to determine the thermal parameters of the Pt/GdIG system. A simulated time-dependent x-ray intensity was calculated from the results of the thermal diffusion simulation by computing the depth average of the temperature and then calculating the change in intensity. The temperature dependence of the diffracted intensity was

calculated using the temperature from the thermal simulation by assuming that the intensity $I(T)$ is proportional to the Debye–Waller factor $e^{-Q^2\sigma^2(T)}$, where Q is the x-ray scattering vector for the Pt 111 reflection and $\sigma^2(T)$ is the mean square displacement. Reported temperature-dependent values of $\sigma^2(T)$ for Pt were used for this calculation.[31,55,56]

The temperature increases arising in the Debye–Waller analysis in Fig. 5(a) are consistent with the temperature increase required to produce the strain resulting from the corresponding 1 mJ cm^{-2} laser fluence in Fig. 1(e). The time dependences of the two measurements are also similar. The conduction of the thermal energy into the substrate is apparent in both Fig. 1(e), as a change in the strain, and Fig. 5(a), as a change in intensity. The slow decrease in ε_{zz} in Fig. 1(e) corresponds to a change in strain at 30 ps by ~0.04% compared to its value immediately after excitation. The decrease in temperature determined from this strain would be ~45 K, which is consistent with the Debye–Waller analysis.

The RMSD was calculated for a range of values of $m_{Pt/GdIG}$ and n from measured and predicted intensity variation with time calculated from the Debye–Waller factor. The RMSD map as a function of $m_{Pt/GdIG}$ and n is shown in Fig. 5(b). The minimum value of RMSD was obtained for $m_{Pt/GdIG} = 0.0036$ GW m^{-2} K^{-1} and $n = 0.8$. Pairs of values of $m_{Pt/GdIG}$ from approximately 0.0045 to 0.002 and of n from 0.7 to 1 have RMSDs that are close to the global minimum. A solid line plots the temperature dependence of $h_{Pt/GdIG}$ with $m_{Pt/GdIG} = 0.0036$ GW m^{-2} K^{-1} and $n = 0.8$ in Fig. 5(c). The shaded region in Fig. 5(c) corresponds to the ranges of $h_{Pt/GdIG}$ calculated with values of $m_{Pt/GdIG}$ and n giving RMSDs near the minimum.

Values of the thermal conductance of Rh/Al_2O_3 and Al/Al_2O_3 interfaces reported in previous studies are also plotted in Fig. 5(c) for comparison with the Pt/GdIG results.[57] The comparison shows that the temperature dependence has a similar trend. We can also compare these results with our previous study, which analyzed the thermal transport using a linear temperature dependence of $h_{Pt/GdIG}$, corresponding to $n = 1$.[18] The current study suggests that the linear temperature dependence is a higher limit on the temperature dependence of $h_{Pt/GdIG}$. The intensity measurements presented here place a precise limit on the temperature dependence of $h_{Pt/GdIG}$, shown in Fig. 5(c).

The experimental results were also compared with a computational study considering the phonon transmittance of the Pt/GdIG interface, using the model shown schematically in Fig. 6(a).[9] A complete description of the interface would include the combination of phonon transmittance with a detailed balance considering the phonon properties of both layers. Here, however, we used the single parameter ε as an effective/reduced descriptor for interfacial phonon transport. The calculation considers the time-dependent phonon population distribution $g(t,z,\omega)$, which is a function of t, depth z, and phonon frequency ω, in the Pt layer using the one-dimensional (1D) phonon Boltzmann transport equation:[9]

$$\frac{\partial g(t,z,\omega)}{\partial t} + \cos(\varphi) v_g(\omega) \frac{\partial g(t,z,\omega)}{\partial z} = -\frac{g(t,z,\omega) - g^{eq}(T(t,z),\omega)}{\tau(\omega)}.$$

Here, $v_g(\omega)$ is the magnitude of the frequency-dependent group velocity vector $v_g(\omega)$ shown in Fig. 6(a), $\tau(\omega)$ is the frequency-dependent relaxation time, and $\varphi \in [0, \pi]$ is the angle between the direction of

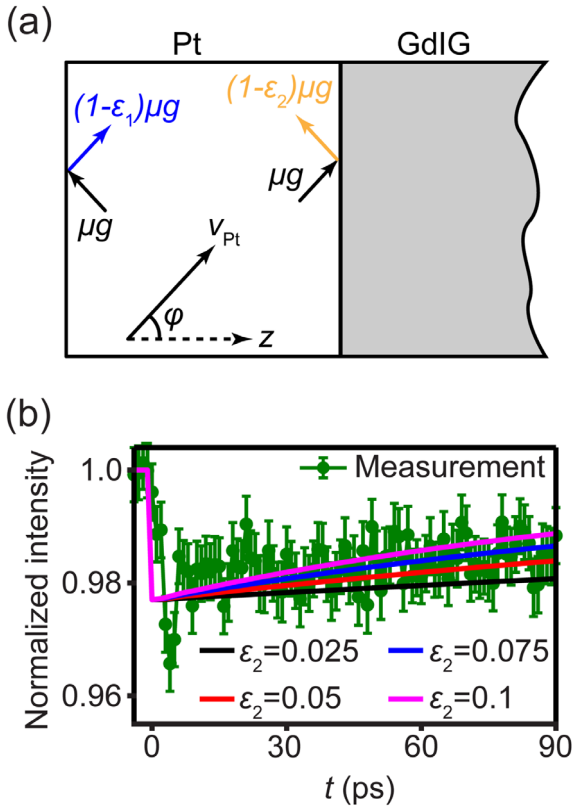

FIG. 6. (a) Schematic of the phonon transport simulation. The phonon population $g(t,z,\omega)$ is denoted as g. The group velocity is v_{Pt}. The $z = 0$ and $z = L_z$ boundary conditions are diffuse reflections of left-going and right-going phonons with energy loss described as $\varepsilon_1 = 0$ and ε_2, respectively. (b) Comparison of results of simulation (lines) with experimentally observed time dependence of the intensity for different values of the interface phonon transmittance ε_2, for a $T_{initial} = 40$ K and 1 mJ cm^{-2} optical fluence.

$v_g(\omega)$ and the z axis to account for all solid angles in the 1D model. The phonon energy distribution is as follows:[9]

$$g(t,z,\omega) = \frac{1}{4\pi}\hbar\omega D(\omega) f(t,z,\omega),$$

where $f(t,z,\omega)$ is the phonon population and $D(\omega)$ is the density of states. The equilibrium energy distribution $g^{eq}(T(t,z),\omega)$ corresponds to the Bose–Einstein distributed phonon population (i.e., $f^{eq} = 1/\left[\exp\left(\frac{\hbar\omega}{k_B T(t,z)}\right) - 1\right]$) given the local temperature $T(t,z)$. The phonon density of states was determined using the Debye model and the reported Debye temperature $T_{D,\,Pt} = 246$ K. The group velocity was taken to be the literature longitudinal acoustic sound velocity of Pt, $v_{Pt} = 3920$ m s^{-1}. The relaxation time was $\tau = \Gamma_{Pt}/v_{Pt}$ given by the mean free path Γ_{Pt} determined above.

The Pt/vacuum interface at $z = 0$ was modeled using a diffuse boundary condition such that all outgoing phonon energies μ are reflected diffusely

$$g(z = 0, \mu > 0) = \varepsilon_1\, g^{eq}(T_0) - 2(1 - \varepsilon_1) \int_{-1}^{0} v_g\, g(z = 0, \mu)\, \mu\, d\mu.$$

The transmission coefficient at $z = 0$ is $\varepsilon_1 = 0$. The Pt/GdIG interface at $z = L_z$ was also described as diffusely reflecting, with energy transmission $0 < \varepsilon_2 < 1$. We assume that no energy is transported from the GdIG to Pt. This assumption is reasonable because the Pt layer has a much higher temperature rise than the GdIG layer such that the energy is transferred into the GdIG layer from Pt but not from GdIG into Pt. The expression for the Pt/GdIG interface is

$$g(z = L_z, \mu < 0) = \varepsilon_2\, g^{\mathrm{eq}}(T_0) + 2(1 - \varepsilon_2) \int_{-1}^{0} g(z = L_z, \mu)\, \mu\, \mathrm{d}\mu.$$

The initial distribution $g(t = 0, z, \omega)$ is an equilibrium distribution with the temperature profile determined using the optical fluence of the pump laser and the thermal parameters of Pt.

The system of equations was discretized in space using the finite volume method with grid size $\Delta z = 0.25$ nm. The time evolution was solved by the forward Euler method with time step $\Delta t = 50$ fs. The computational details can be found in the supplementary material of Ref. 9.

A comparison of the results of the simulation with the experimentally measured intensity is shown in Fig. 6(b). The best agreement is obtained with a value of $\varepsilon_2 = 0.05$, corresponding to a phonon transmittance of 0.05 at the Pt/GdIG interface, with values of 0.025 and 0.075 providing notably worse agreement. The uncertainty due to counting statistics did not affect this estimate of ε_2. The best agreement, $\varepsilon_2 = 0.05$, corresponds to a reflectance of 0.95. In comparison, the acoustic amplitude reflectance measured above for the strain pulse was 0.28, corresponding to a power reflectance of 0.08. The contrasting observation of purely diffuse phonon reflection at the Pt interface for thermal transport and highly specular reflection for the acoustic propagation above is a result of the difference in relevant phonon frequencies. The difference between the relatively low reflectance of the low-frequency acoustic pulse and the higher reflectance (corresponding to low ε_2) at the higher THz-range frequencies of heat transport may also arise from the frequency-dependent mismatch between the acoustic properties of Pt and GdIG. Further experiments may narrow the time-domain difference between the range of acoustic and thermal experiments.

IV. CONCLUSION

The acoustic and thermal properties of Pt/GdIG heterostructures have immediate consequences for the design of materials, interfaces, and devices for spincaloritronics. These devices depend fundamentally on linking a heat current mediated by phonons to a current of magnetic excitations mediated by magnons.[19] The temperature profile and heat flux are separate but important parameters of emerging descriptions of the spin-Seebeck effect.[58] The thermal parameters determined here are relevant to the heat transfer between a heated Pt layer and GdIG, helping to provide the temperature distribution within the GdIG layer in spin-Seebeck models. The temperature changes determined using the lattice expansion, Debye–Waller analysis, and estimates of the energy absorbed from the optical pulse are all mutually consistent, pointing to future opportunities to use these methods in complementary ways during ultrafast thermal transport experiments.

More generally, thermal transport phenomena provide the means to observe phase transformation physics and dynamics via the coupling among the electronic, lattice, and magnetic degrees of freedom of materials. Phonon lifetimes and transition rates for specific processes are the keys to steps such as the generation of Floquet states and the manipulation of specific modes linked to phase transformations.[59,60] The crossover between coherent phonon dynamics and thermal transport occurs in a range of phonon frequencies, layer thicknesses, and lifetimes in the THz range that are accessible via time-resolved x-ray diffraction methods.[1,61] The results here provide insight into the specific predictions of atomic-to-mesoscopic descriptions of acoustic properties and interface thermal phenomena and provide a combined experimental/analysis method that can be used to provide insight into other systems. Further directions include the coupling of the acoustic pulse to the spin-wave modes of the GdIG layer, the dynamics and damping of magnetoelastic modes, and magnon–phonon hybridization.[62–64]

ACKNOWLEDGMENTS

This work was supported by the U.S. Department of Energy, Basic Energy Sciences, under Contract No. DE-FG02-04ER46147. Use of the Linac Coherent Light Source (LCLS), SLAC National Accelerator Laboratory, is supported by the U.S. Department of Energy, Office of Science, Office of Basic Energy Sciences under Contract No. DE-AC02-76SF00515. M.L. acknowledges the National Science Foundation (NSF) Designing Materials to Revolutionize and Engineer our Future (DMREF) Program with Award No. DMR-2118448.

AUTHOR DECLARATIONS

Conflict of Interest

The authors have no conflicts to disclose.

Author Contributions

Deepankar Sri Gyan: Conceptualization (equal); Data curation (equal); Formal analysis (equal); Investigation (equal); Methodology (equal); Validation (equal); Visualization (equal); Writing – original draft (equal); Writing – review & editing (equal). **Ni Li:** Conceptualization (equal); Data curation (equal); Investigation (equal); Methodology (equal); Writing – original draft (equal). **Zhantao Chen:** Conceptualization (equal); Formal analysis (equal); Methodology (equal); Writing – review & editing (equal). **Stephan Geprägs:** Investigation (equal); Methodology (equal); Writing – review & editing (equal). **Maxim Dietlein:** Investigation (equal); Methodology (equal). **Rudolf Gross:** Formal analysis (equal); Investigation (equal); Methodology (equal); Project administration (equal). **Takahiro Sato:** Conceptualization (equal); Data curation (equal); Formal analysis (equal); Investigation (equal); Methodology (equal); Writing – review & editing (equal). **Yanwen Sun:** Investigation (equal); Methodology (equal); Writing – review & editing (equal). **Matthias C. Hoffmann:** Investigation (equal); Methodology (equal). **Diling Zhu:** Conceptualization (equal); Investigation (equal); Methodology (equal); Writing – review & editing (equal). **Daniel Haskel:** Conceptualization (equal); Investigation (equal); Methodology (equal); Writing – review & editing (equal). **Jörg Strempfer:** Conceptualization (equal); Investigation (equal); Methodology (equal); Writing – review & editing (equal). **Mingda Li:** Conceptualization (equal); Formal analysis (equal); Investigation (equal); Methodology (equal); Writing – original draft (equal); Writing – review & editing (equal). **Danny Mannix:**

Conceptualization (equal); Formal analysis (equal); Funding acquisition (equal); Investigation (equal); Project administration (equal); Writing – original draft (equal); Writing – review & editing (equal). **Paul G. Evans:** Conceptualization (equal); Data curation (equal); Funding acquisition (equal); Investigation (equal); Methodology (equal); Project administration (equal); Supervision (equal); Visualization (equal); Writing – original draft (equal); Writing – review & editing (equal).

DATA AVAILABILITY

The data that support the findings of this study are available from the corresponding author upon reasonable request.

REFERENCES

[1]M. V. Simkin and G. D. Mahan, Phys. Rev. Lett. **84**(5), 927–930 (2000).
[2]J. Chen, X. F. Xu, J. Zhou, and B. W. Li, Rev. Mod. Phys. **94**(2), 50 (2022).
[3]D. G. Cahill, W. K. Ford, K. E. Goodson, G. D. Mahan, A. Majumdar, H. J. Maris, R. Merlin, and S. R. Phillpot, J. Appl. Phys. **93**(2), 793–818 (2003).
[4]D. G. Cahill, P. V. Braun, G. Chen, D. R. Clarke, S. H. Fan, K. E. Goodson, P. Keblinski, W. P. King, G. D. Mahan, A. Majumdar, H. J. Maris, S. R. Phillpot, E. Pop, and L. Shi, Appl. Phys. Rev. **1**(1), 45 (2014).
[5]Q. Li, F. Liu, S. Hu, H. Song, S. Yang, H. Jiang, T. Wang, Y. K. Koh, C. Zhao, and F. Kang, Nat. Commun. **13**(1), 4901 (2022).
[6]J. Wang, Z. Wang, K. Yang, N. Chen, J. Ni, J. Song, Q. Li, F. Sun, Y. Liu, and T. Fan, Adv. Funct. Mater. **32**(40), 2206545 (2022).
[7]B. Zhao, Y. Qu, W. Zhao, and Y. Deng, Mater. Today Phys. **42**, 101379 (2024).
[8]A. Giri, S. G. Walton, J. Tomko, N. Bhatt, M. J. Johnson, D. R. Boris, G. Lu, J. D. Caldwell, O. V. Prezhdo, and P. E. Hopkins, ACS Nano **17**(15), 14253–14282 (2023).
[9]Z. T. Chen, X. Z. Shen, N. Andrejevic, T. T. Liu, D. Luo, T. Nguyen, N. C. Drucker, M. E. Kozina, Q. C. Song, C. Y. Hua, G. Chen, X. J. Wang, J. Kong, and M. D. Li, Adv. Mater. **35**(2), 2206997 (2023).
[10]M. Först, R. Mankowsky, H. Bromberger, D. M. Fritz, H. Lemke, D. Zhu, M. Chollet, Y. Tomioka, Y. Tokura, R. Merlin, J. P. Hill, S. L. Johnson, and A. Cavalleri, Solid State Commun. **169**, 24–27 (2013).
[11]S. L. Johnson, M. Savoini, P. Beaud, G. Ingold, U. Staub, F. Carbone, L. Castiglioni, M. Hengsberger, and J. Osterwalder, Struct. Dyn. **4**(6), 061506 (2017).
[12]M. Chollet, R. Alonso-Mori, M. Cammarata, D. Damiani, J. Defever, J. T. Delor, Y. Feng, J. M. Glownia, J. B. Langton, and S. Nelson, J. Synchrotron Radiat. **22**(3), 503–507 (2015).
[13]H. Enquist, A. Jurgilaitis, A. Jarnac, Å. Bengtsson, M. Burza, F. Curbis, C. Disch, J. C. Ekström, M. Harb, and L. Isaksson, Synchrotron Radiat. **25**(2), 570–579 (2018).
[14]A. Koç, C. Hauf, M. Woerner, L. von Grafenstein, D. Ueberschaer, M. Bock, U. Griebner, and T. Elsaesser, Opt. Lett. **46**(2), 210–213 (2021).
[15]P. Klemens, Int. J. Thermophys. **2**, 55–62 (1981).
[16]C. Thomsen, H. T. Grahn, H. J. Maris, and J. Tauc, Phys. Rev. B **34**(6), 4129 (1986).
[17]H. J. Lee, Y. Ahn, S. D. Marks, E. C. Landahl, S. H. Zhuang, M. H. Yusuf, M. Dawber, J. Y. Lee, T. Y. Kim, S. Unithrattil, S. H. Chun, S. Kim, I. Eom, S. Y. Park, K. S. Kim, S. Lee, J. Y. Jo, J. M. Hu, and P. G. Evans, Phys. Rev. X **11**(3), 031031 (2021).
[18]D. Sri Gyan, D. Mannix, D. Carbone, J. L. Sumpter, S. Geprägs, M. Dietlein, R. Gross, A. Jurgilaitis, V.-T. Pham, and H. Coudert-Alteirac, Struct. Dyn. **9**(4), 045101 (2022).
[19]S. Geprägs, A. Kehlberger, F. D. Coletta, Z. Qiu, E.-J. Guo, T. Schulz, C. Mix, S. Meyer, A. Kamra, and M. Althammer, Nat. Commun. **7**(1), 10452 (2016).
[20]J. Yang, L. Xi, W. Qiu, L. Wu, X. Shi, L. Chen, J. Yang, W. Zhang, C. Uher, and D. J. Singh, npj Comput. Mater. **2**(1), 1–17 (2016).
[21]M. Levenson and E. Sawatzky, J. Appl. Phys. **40**(6), 2672–2673 (1969).
[22]A. Y. Yu, W. Spicer, and G. Hass, Phys. Rev. **171**(3), 834 (1968).
[23]D. Zahn, H. Seiler, Y. W. Windsor, and R. Ernstorfer, Struct. Dyn. **8**(6), 064301 (2021).
[24]A. Giri and P. E. Hopkins, Adv. Funct. Mater. **30**(8), 1903857 (2020).
[25]M. Harmand, R. Coffee, M. R. Bionta, M. Chollet, D. French, D. Zhu, D. Fritz, H. Lemke, N. Medvedev, and B. Ziaja, Nat. Photonics **7**(3), 215–218 (2013).
[26]J. Arblaster, Platinum Met. Rev. **38**(3), 119–125 (1994).
[27]R. J. Corruccini and J. J. Gniewek, *Specific Heats and Enthalpies of Technical Solids at Low Temperatures: A Compilation from the Literature* (US Government Printing Office, 1960).
[28]A. Darling, Platinum Met. Rev. **10**(1), 14–19 (1966).
[29]V. Kitaeva, E. Zharikov, and I. Chistyi, Phys. Status Solidi A **92**(2), 475–488 (1985).
[30]G. V. Samsonov, in *Handbook of the Physicochemical Properties of the Elements*, edited by G. V. Samsonov (Springer US, Boston, MA, 1968), pp. 387–446.
[31]N. B. Duc, V. Q. Tho, T. S. Tien, D. Q. Khoa, and H. K. Hieu, Rad. Phys. Chem. **149**, 61–64 (2018).
[32]S. O. Kasap, *Principles of Electronic Materials and Devices* (McGraw-Hill, 2006).
[33]H. Sugawara, S. Sato, T. Miyahara, A. Kakizaki, Y. Morioka, Y. Iguchi, I. Nagakura, M. Ando, T. Ohta, and S. Aoki, Nucl. Instrum. Methods Phys. Res. Sect. A **228**(2–3), 549–555 (1985).
[34]G. K. White, J. Phys. F **2**(2), L30 (1972).
[35]J. Manguele, F. Baudouin, C. Cibert, B. Domengès, V. Demange, M. Guilloux-Viry, A. Fouchet, and G. Poullain, SN Appl. Sci. **2**, 1–10 (2020).
[36]J. Arblaster, Platinum Met. Rev. **41**(1), 12–21 (1997).
[37]M. Mattern, A. von Reppert, S. P. Zeuschner, M. Herzog, J.-E. Pudell, and M. Bargheer, Photoacoustics **31**, 100503 (2023).
[38]D. Schick, M. Herzog, A. Bojahr, W. Leitenberger, A. Hertwig, R. Shayduk, and M. Bargheer, Struct. Dyn. **1**(6), 064501 (2014).
[39]P. Ding, Y. Zhu, Z. Han, L. Li, L. Zhang, Y. Cai, D. J. Singh, L. Zhang, W. Zhang, S. Shin, J. Yang, W. Liu, and L. Guo, Phys. Rev. B **108**(6), 064310 (2023).
[40]J. H. Hodak, A. Henglein, and G. V. Hartland, J. Chem. Phys. **111**(18), 8613–8621 (1999).
[41]J. M. Lilly and S. C. Olhede, IEEE Trans. Signal Process. **60**(11), 6036–6041 (2012).
[42]J. M. Lilly, Proc. R. Soc. A **473**(2200), 20160776 (2017).
[43]K. W. Böer and U. W. Pohl, *Semiconductor Physics* (Springer Nature, 2023).
[44]J. Franklin, *Mathematical Methods for Oscillators and Waves* (Cambridge University Press, 2020).
[45]C. Kittel and P. McEuen, *Introduction to Solid State Physics* (John Wiley & Sons, 2018).
[46]N. Del Fatti, C. Voisin, F. Chevy, F. Vallée, and C. Flytzanis, J. Chem. Phys. **110**(23), 11484–11487 (1999).
[47]M. Kanskar and M. N. Wybourne, Phys. Rev. B **50**(1), 168–172 (1994).
[48]J. Zou and A. Balandin, J. Appl. Phys. **89**(5), 2932–2938 (2001).
[49]E. Ma, *Chemistry and Physics of Nanostructures and Related Non-Equilibrium Materials* (Minerals Metals and Materials Society, 1997).
[50]O. Gupta and H. Kharoo, J. Chem. Phys. **74**(6), 3577–3583 (1981).
[51]K. Atkinson, *An Introduction to Numerical Analysis* (John Wiley & Sons, 1991).
[52]G. White and S. Woods, Can. J. Phys. **35**(3), 248–257 (1957).
[53]R. Iguchi, K.-I. Uchida, S. Daimon, and E. Saitoh, Phys. Rev. B **95**(17), 174401 (2017).
[54]E. Gmelin, M. Asen-Palmer, M. Reuther, and R. Villar, J. Phys. D **32**(6), R19 (1999).
[55]L. A. Bertolo and M. M. Shukla, Phys. Status Solidi B **77**(2), 433–439 (1976).
[56]K. N. Mehrotra and J. P. Dixit, Acta Phys. Acad. Sci. Hung. **46**(1), 27–30 (1979).
[57]Y. R. Koh, J. Shi, B. Wang, R. Hu, H. Ahmad, S. Kerdsongpanya, E. Milosevic, W. A. Doolittle, D. Gall, and Z. Tian, Phys. Rev. B **102**(20), 205304 (2020).
[58]T. Kikkawa and E. Saitoh, Ann. Rev. Condens. Matter Phys. **14**, 129–151 (2023).
[59]M. Rodriguez-Vega, M. Vogl, and G. A. Fiete, Ann. Phys. **435**, 168434 (2021).
[60]P. G. Radaelli, Phys. Rev. B **97**(8), 085145 (2018).
[61]J. Ravichandran, A. K. Yadav, R. Cheaito, P. B. Rossen, A. Soukiassian, S. J. Suresha, J. C. Duda, B. M. Foley, C.-H. Lee, Y. Zhu, A. W. Lichtenberger, J. E. Moore, D. A. Muller, D. G. Schlom, P. E. Hopkins, A. Majumdar, R. Ramesh, and M. A. Zurbuchen, Nat. Mater. **13**(2), 168–172 (2014).
[62]C. Kittel, Phys. Rev. **110**(4), 836–841 (1958).
[63]A. Rückriegel, P. Kopietz, D. A. Bozhko, A. A. Serga, and B. Hillebrands, Phys. Rev. B **89**(18), 184413 (2014).
[64]S. Streib, N. Vidal-Silva, K. Shen, and G. E. W. Bauer, Phys. Rev. B **99**(18), 184442 (2019).